SCIENTIFIC REPORTS
nature research

OPEN

$FeCoSe_2$ Nanoparticles Embedded in g-C_3N_4: A Highly Active and Stable bifunctional electrocatalyst for overall water splitting

Muhammad Zulqarnain[1], Afzal Shah[1,3*], Muhammad Abdullah Khan[2], Faiza Jan Iftikhar[4] & Jan Nisar[5]

To investigate cost affordable and robust HER and OER catalysts with significant low overpotentials, we have successfully embedded $FeCoSe_2$ spheres on smooth surfaces of graphitic carbon nitride that demonstrated high stability and electrocatalytic activity for H_2 production. We systematically analyzed the composition and morphology of $Fe_xCo_{1-x}Se_2$/g-C_3N_4 and attributed the remarkable electrochemical performance of the catalyst to its unique structure. $Fe_{0.2}Co_{0.8}Se_2$/g-C_3N_4 showed a superior HER activity, with quite low overpotential value (83 mV at −20 mA cm^{-2} in 0.5 M H_2SO_4) and a current density of −3.24, −7.84, −14.80, −30.12 mA cm^{-2} at 0V (vs RHE) in Dulbecco's Phosphate-Buffered Saline (DPBS), artificial sea water (ASW), 0.5 M H_2SO_4 and 1 M KOH, respectively. To the best of our knowledge, these are the highest reported current densities at this low potential value, showing intrinsic catalytic activity of the synthesized material. Also, the catalyst was found to deliver a high and stable current density of −1000 mA cm^{-2} at an overpotential of just 317 mV. Moreover, the synthesized catalyst delivered a constant current density of −30 mA cm^{-2} for 24 h without any noticeable change in potential at −0.2V. These attributes confer our synthesized catalyst to be used for renewable fuel production and applications.

Significant increase in the fossil fuel consumption and associated environmental threats of greenhouse gases have urged the scientific community to explore a sustainable and everlasting source of energy[1]. The fuel cell technology is considered as an efficient, long-lasting and environmental friendly source of energy. Among various existing forms of fuel cells, the H_2/O_2 fuel cells are deemed as zero carbon discharging technology with only water as the combustion product[2,3]. To ensure higher cell efficiency, the supply of pure fuel is essential and water electrolysis is one of the most convenient ways of producing H_2. In fact, water splitting has garnered enough spotlight because of the highly pure and plentiful supply of fuel produced during this process. Likewise, this strategy does not demand elevated temperatures and pressure reactors. The overall water electrolysis can be explained by the following two half-cell reactions: hydrogen evolution reaction (HER) at the cathode[4,5] and oxygen evolution reaction (OER) at the anode[6,7], investigated in acidic and alkaline conditions, respectively[5,8].

$$2H^{+}_{(aq)} + 2e^{-} \rightarrow H_{2(g)}$$

$$4OH^{-}_{(aq)} \rightarrow 2H_2O_{(l)} + O_{2(g)} + 4e^{-}$$

The noble metals i.e., Platinum for HER[9–14] and Iridium or Ruthenium for OER[15–18] being expensive and scarce, must be substituted by earth abundant and cost effective non-noble metals[19] or metal free catalysts such

[1]Department of Chemistry Quaid-i-Azam University, 45320, Islamabad, Pakistan. [2]Renewable Energy Advancement laboratory, Department of Environmental Sciences, Quaid-i-Azam University, 45320, Islamabad, Pakistan. [3]Department of Chemistry, College of Science, University of Bahrain, Sakhir, 32038, Kingdom of Bahrain. [4]NUTECH School of Applied Sciences and Humanities, National University of Technology, Islamabad, 44000, Pakistan. [5]National Centre of Excellence in Physical Chemistry, University of Peshawar, Peshawar, 25120, Pakistan. *email: afzals_qau@yahoo.com

as carbon based electrocatalysts. This work is an effort to substitute the expensive noble metals with only a small amount of earth abundant and cost effective non-noble metal catalysts to achieve better HER activity than the commercial catalysts reported so far. Among the metal free substrates, Carbon Nitride (C_3N_4) is the best choice as it offers π-conjugated graphitic planner layers with good conductivity and large surface area[20,21]. The C_3N_4 is reported as one of the primitive synthetic polymeric materials that offers different ways to modify its reactivity without any change in composition[22–28]. The g-C_3N_4 is believed to possess N-bridged poly(tri-s-triazine) planar structure with high degree of condensation. The s-triazine framework makes it thermally (up to 600 °C) and chemically stable. Moreover, it is a semiconducting material of medium band gap value (2.7 eV) that finds extensive use as a photo(electro)catalyst[29–33].

Recently, transition-metals sulfides, phosphides and selenides have been found to be efficient HER catalysts[34,35]. Likewise, various electrocatalysts including metal alloys[36,37], metal nitrides[38,39], metal phosphides[40], metal carbides[41], metal dichalcogenides[42] and carbon-based catalysts have also attracted attention of researchers in the last few years[43,44]. The transition metal dichalcogenides (TMDs) have been found to be promising water splitting electrocatalysts and have thus gained significant interest in technological applications due to their unique electronic structure, different chemical compositions and diverse crystal symmetry. Several routes i.e. homogeneously dispersed electrocatalyst on conductive supports, chemical vapor and electron beam deposition have been developed to exploit the electrocatalytic properties of these materials[45–47]. However, the above-mentioned synthetic approaches are unfeasible for large scale production as control over the layers, chirality and influence of different substrates on its fabrication is still an area that is not well explored. The chemical doping is considered as an important structure-engineering technique to increase active sites and conductivity of these electrocatalysts[48] which will be explored in this work.

Previously, Transition metal dichalcogenides (TMDs) such as NiS_2, FeS_2, and CoS_2 displayed efficient overall water splitting performance[49–51]. Similarly, Iron (Fe) found in its natural form such as Nitrogenases and Hydrogenase (natural hydrogen evolution enzymatic catalysts) is the most promising material for HER. Hence, Iron doping is expected to increase the electrocatalytic performance of HER catalysts. Similarly, sulfur component of above-mentioned catalysts can be replaced with selenium. Sulfur and selenium are present in the same group and both exhibit similar properties, but selenides are expected to enhance HER performance of electrocatalysts due to low bond strength of Se–H (276 kJ/mol) than P–H (322 kJ/mol) and S–H (363 kJ/mol). Obviously, the bond strength has a great influence on the extent of adsorption/desorption of the intermediate states during catalysis. The weaker Se–H bond as compared to P–H and S–H is expected to facilitate the product desorption from catalytic sites which circumvents catalyst poisoning and thus stable and efficient performance is projected. Moreover, the Se sites can help to promote the delivery of oxygen molecules because of the localized negative charge of Se sites for OER. Likewise, there is a 3d–2p electronic repulsion amid metal and Se d-band centers[32].

Herein, we have reported a facile method for synthesizing highly active and stable $FeCoSe_2$ on graphitic carbon nitride substrate ($Fe_xCo_{1-x}Se_2$/g-C_3N_4) as novel catalyst for overall water splitting. The catalytic activity of $Fe_xCo_{1-x}Se_2$/g-C_3N_4 significantly improved with increased Fe percentages in the composite material. The $Fe_{0.2}Co_{0.8}Se_2$/g-C_3N_4, has proven itself to be a promising electrocatalyst for HER and OER due to its high conductivity, unique structure and high surface area.

Experimental Section

Chemicals and materials. Iron (III) Nitrate ($Fe(NO_3)_3{\cdot}9\,H_2O$), Cobalt (II) Chloride hexahydrate ($CoCl_2.6H_2O$), Urea ($CO(NH_2)_2$) and Selenium Powder (Se) were purchased from Sigma-Aldrich. Potassium hydroxide, Sulfuric acid and Iso-propanol were of analytical grade and were used as received without any further purification. Preparation of Indian standard artificial sea water (ASW) and Dulbecco's Phosphate-Buffered Saline (DPBS) is detailed in Supplementary note 1.

Synthesis of graphitic carbon nitride. The graphitic carbon nitride was synthesized by using combustion method. The 10 g of urea powder was placed in a covered silica crucible and calcined at 500 °C for 4 h at a heating rate of 2 °C/min. The g-C_3N_4 powder was collected and exfoliated in excess of distilled water for 5 h, dried at 80 °C and stored for further use.

Synthesis of $CoSe_2$ and $Fe_xCo_{1-x}Se_2$ embedded in g-C_3N_4. To synthesize $CoSe_2$ embedded in g-C_3N_4, a simple hydrothermal route was followed. Solution A was prepared by adding 0.8 mmol of cobalt source, 2 ml of 0.5 M aqueous solution of ethylene diamine tetra-acetic acid ligand, and 20 mg of g-C_3N_4. While solution B was prepared by dissolving 1.62 mmol of Se powder in 8 ml of 3.3 M NaOH. Both solutions were mixed by ultrasonication and the mixture was shifted to a Teflon autoclave and maintained at 180 °C for 18 h. While to produce $Fe_xCo_{1-x}Se_2$/g-C_3N_4, cobalt source in the solution A was substituted by appropriate amount of iron nitrate and cobalt chloride solutions. In each case, black product was collected and washed with deionized water followed by air drying for characterizations and application of the as-synthesized product. Total quantity of metal sources (Fe + Co) was kept very low and constant (0.8 mmol). For $Fe_{0.2}Co_{0.8}Se_2$/g-C_3N_4, the molar ratio of Fe, Co, and Se was maintained at 1: 4: 10. Finally, feeding ratios of metals were further confirmed by average results of EDX (Energy Dispersive X-ray Spectroscopy).

Fabrication of electrodes. 3 mg of each sample and 20 μL of 5 wt.% Nafion were dispersed in 80 μL of iso-propanol to make a slurry. Then 5 μL of slurry was drop casted on glassy carbon electrode (GCE) of geometric surface area of 0.0707 cm^2 and dried in air. These fabricated electrodes (with mass loading of 2.12 mg cm^{-2}) were used as cathodes and anodes for respective electrochemical measurements of HER and OER respectively.

Characterization. To identify the crystalline structure of products, X-ray diffraction (XRD) was performed on Rigaku D/max 2500 with a Cu Kα1 radiation source (λ = 1.54056 Å). Morphologies of prepared samples were

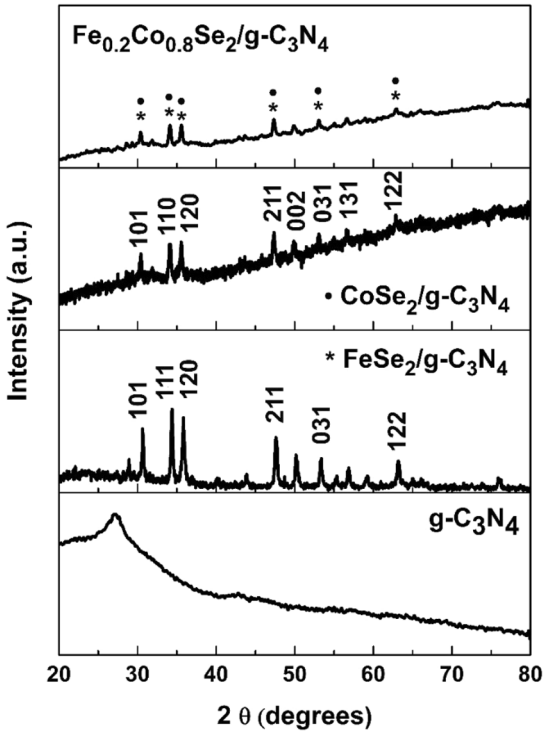

Figure 1. Powder X-ray diffraction pattern of g-C_3N_4, $FeSe_2$/g-C_3N_4, $CoSe_2$/g-C_3N_4, and $Fe_{0.2}Co_{0.8}Se_2$/g-C_3N_4.

identified at Hitachi S-4800 Scanning Electron Microscope (SEM) at an accelerating voltage of 30 KV. Energy dispersive X-ray spectra (EDX) were observed on an Oxford Material Analysis equipped on SEM and Transmission electron microscopy (TEM). While, Fourier Transform Infra-Red (FTIR) spectroscopic measurements were carried on TENSOR-27 (Bruker) and differential scanning calorimetry/thermal gravimetric analysis (DSC/TGA) on TA SDT Q600.

Electrochemical measurements. Electrochemical studies were carried out on Autolab PGSTAT302N Metrohm, (running with NOVA 1.11 software) electrochemical workstation at room temperature. While, EIS measurement was made with a Gamry EIS 300 electrochemical impedance analyzer with frequencies ranging from 100 kHz to 0.1 Hz at a voltage amplitude of 10 mV. The electrocatalytic ability of all materials was studied in 0.5 M H_2SO_4, DPBS, ASW, and in 1 M KOH for HER using a three-electrode configuration at a scan rate of 20 mV/s. The $Fe_xCo_{1-x}Se_2$/g-C_3N_4 powder on GCE was used as working, Platinum (Pt) wire as counter and Ag/AgCl (sat. KCl) as reference electrode. All potentials in this work are reported versus Reversible Hydrogen electrode (RHE) according to the Eq. 1.

$$E(RHE) = E(Ag/AgCl) + 0.197 + (0.059 \times pH) \quad (1)$$

Results and Discussion

The Fe/Co ratio was controlled, and a series of samples were prepared. The effect of Fe/Co ratio on the composition and the crystalline phase was investigated by X-ray diffraction (XRD) technique and is shown in Fig. 1. The diffraction peaks at 30.6, 34.4, 35.7, 47.7 and 50.3 match well and can be indexed to the planes of powder diffraction standard database of $CoSe_2$ (JCPDS # 53- 0449) and $FeSe_2$ (JCPDS # 21- 0432), respectively. It is noteworthy that the diffraction peaks of g-C_3N_4 are not indexable in the $Fe_{0.2}Co_{0.8}Se_2$/g-C_3N_4 partly due to their comparatively low diffraction intensity, as carbon nitride synthesized from urea shows low diffraction intensity, and partly to relatively small amount of carbon nitride present in the sample. In addition, with increase in Fe amount, the intensity of XRD signals decreased which implied low crystallinity of the $Fe_{0.2}Co_{0.8}Se_2$/g-C_3N_4 material in comparison to the pristine ones. Furthermore, the final product ($Fe_{0.2}Co_{0.8}Se_2$/g-C_3N_4) showed diffraction peaks corresponding to both $CoSe_2$, and $FeSe_2$, which indicates the coexistence of the two orthorhombic phases[52]. It is pertinent to mention here that owing to the small differences in ionic radii of iron and cobalt, the strongest diffraction peaks of $FeCoSe_2$, $FeSe_2$ and $CoSe_2$ displayed very little interlayer spacing difference (±0.01 Å), which provided the basis for facile doping of Fe into the $CoSe_2$ structures. Additionally, Fourier transform infrared spectroscopy (FTIR) was conducted to reveal the bonding states of $Fe_xCo_{1-x}Se_2$/g-C_3N_4 samples (Fig. S1).

The morphologies of all samples were studied by SEM (Fig. 2). The Fe free material ($CoSe_2$/g-C_3N_4) exhibited a not so well-defined nodular morphology (Figs. 2a and S2a), however, after the addition of Fe, $Fe_{0.2}Co_{0.8}Se_2$/g-C_3N_4 showed a similar morphology to $CoSe_2$/g-C_3N_4 but with the appearance of rather uniform sphere like structures embedded on to the $CoSe_2$ smooth surface (Fig. 2b). In addition, Fig. 2b depicts a porous framework of $Fe_{0.2}Co_{0.8}Se_2$/g-C_3N_4 electrocatalyst, which is favorable for catalytic applications. Whereas, in the case of

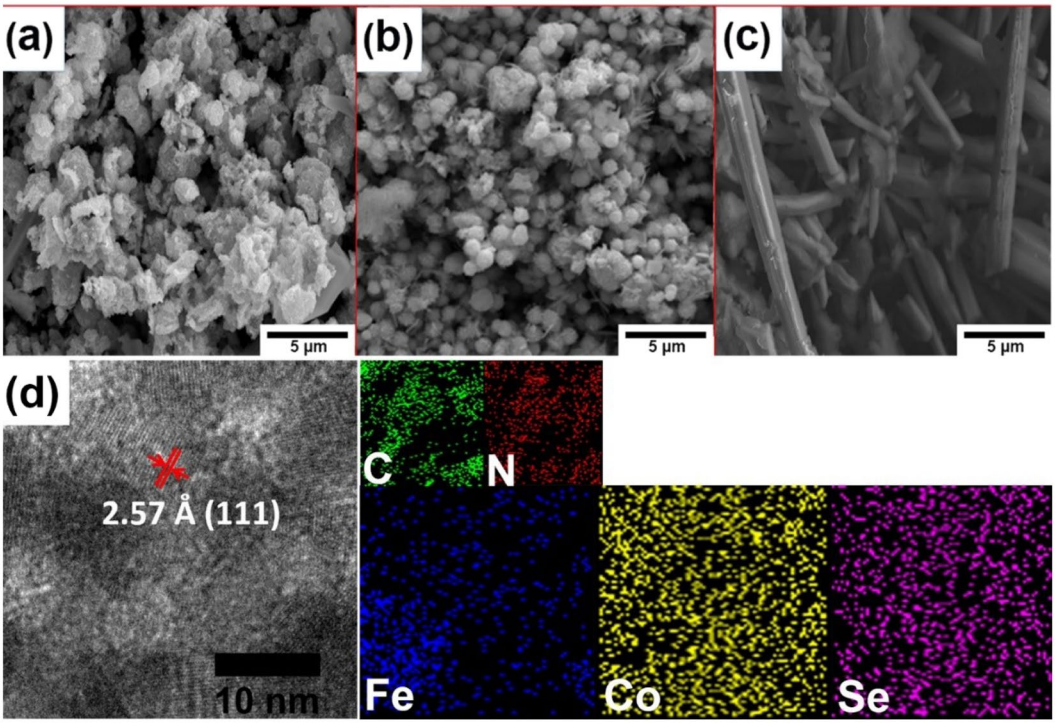

Figure 2. SEM micrographs of (**a**) $CoSe_2/g\text{-}C_3N_4$ (**b**) $Fe_{0.2}Co_{0.8}Se_2/g\text{-}C_3N_4$ and (**c**) $FeSe_2/g\text{-}C_3N_4$. d) TEM micrograph and elemental mapping images of $Fe_{0.2}Co_{0.8}Se_2/g\text{-}C_3N_4$.

$FeSe_2/g\text{-}C_3N_4$, due to increase in Fe content in $Fe_xCo_{1-x}Se_2/g\text{-}C_3N_4$, a completely different rod type morphology was seen (Figs. 2c and S3). This appearance of distinct morphologies of two metals (Co, Fe) with Se is as result of their different directional growths under hydrothermal conditions. Furthermore, elemental mapping of synthesized material confirmed a fairly uniform distribution of constituent elements (Fig. S2c and Table S1). The TEM image of $Fe_{0.2}Co_{0.8}Se_2/g\text{-}C_3N_4$ (Fig. 2d) shows crystalline nature of the material where fringe analysis reveal that the lattice distances remain same throughout the sample. The spherical shape of $Fe_{0.2}Co_{0.8}Se_2/g\text{-}C_3N_4$, corresponds to the results obtained from SEM.

The as-obtained compounds were further investigated by the simultaneous application of thermogravimetry and differential scanning calorimetry (TG-DSC) to study the effect of temperature, phase transition phenomenon and the associated endothermic or exothermic effects (Figs. S4 and S5). Due to the presence of $g\text{-}C_3N_4$ substrate, the compounds are found to be stable for a wide temperature range. Among these samples, $g\text{-}C_3N_4$ was found to be the most stable one. While comparing $Fe_{0.2}Co_{0.8}Se_2$ and $Fe_{0.2}Co_{0.8}Se_2/g\text{-}C_3N_4$, it is clear that $g\text{-}C_3N_4$ has a significant effect on the thermal stability of prepared samples. DSC studies of $g\text{-}C_3N_4$ reveal that it undergoes an exothermic phase transition in the temperature range of 675–725 °C. Whereas, $Fe_{0.2}Co_{0.8}Se_2/g\text{-}C_3N_4$ first shows an endothermic transition at 425.6 °C and then an exothermic phase transition at 580 °C. All the samples were further investigated for electrocatalytic overall water splitting performance.

Electrocatalytic water splitting performance. The HER performance of the prepared samples $Fe_xCo_{1-x}Se_2/g\text{-}C_3N_4$ (x = 0, 0.2, 0.4, 0.6, 0.8 and 1) were investigated in 0.5 M H_2SO_4, DPBS, ASW and 1 M KOH. The best electrocatalytic performance was observed for $Fe_{0.2}Co_{0.8}Se_2/g\text{-}C_3N_4$. Fig. S6a compares the HER activity of the materials of all composition without iR compensation in 0.5 M H_2SO_4. The $Fe_{0.2}Co_{0.8}Se_2/g\text{-}C_3N_4$ showed best electrocatalytic activity with highest current density values of −14.8, −20, −100 mA cm^{-2} at potential values of 0, 83, and 209 m V respectively in 0.5 M H_2SO_4 solution. As HER is facilitated in acidic medium, the current density of −14.8 mA cm^{-2} is likely due to the formation of $HSeO_3^-$ in strong acidic conditions and its subsequent reduction to H_2Se and or HSe^- [53]. To further explore the role of acid, HER was also carried out in DPBS solution where $FeCoSe_2$ exhibited a low current density value of −3.24 mA cm^{-2}, confirming the role of acid in the formation and reduction of $HSeO_3^-$ (Fig. S6b)[5]. Basu *et al.* have reported similar results by employing $CoSe_2/C_3N_4$ catalyst which displayed a photocurrent density of −4.89 mA cm^{-2} [54]. The Fig. 3a presents the comparison of $Fe_{0.2}Co_{0.8}Se_2/g\text{-}C_3N_4$ with $CoSe_2/g\text{-}C_3N_4$, $g\text{-}C_3N_4$ substrate, and Pt after iR compensation. The poor electrocatalytic HER activity of $g\text{-}C_3N_4$ suggests that the major role for higher HER activity is not coming from the substrate itself but it helps in the dispersion of $Fe_xCo_{1-x}Se_2$ onto the smooth surface of $g\text{-}C_3N_4$.

While $CoSe_2/g\text{-}C_3N_4$ showed comparatively good performance with overpotentials of 193 mV, 450 mV at −20 and −100 mA cm^{-2} respectively than $g\text{-}C_3N_4$, the introduction of iron further enhanced the electrocatalytic activity. Therefore, by adjusting the feed ratio, highest and stable HER performance for $Fe_{0.2}Co_{0.8}Se_2/g\text{-}C_3N_4$ with a current density as high as −1000 mA cm^{-2} was achieved without significant interference from the produced H_2 bubbles. The negligible interference from the H_2 bubbles ensures that the modified electrode favors the fast

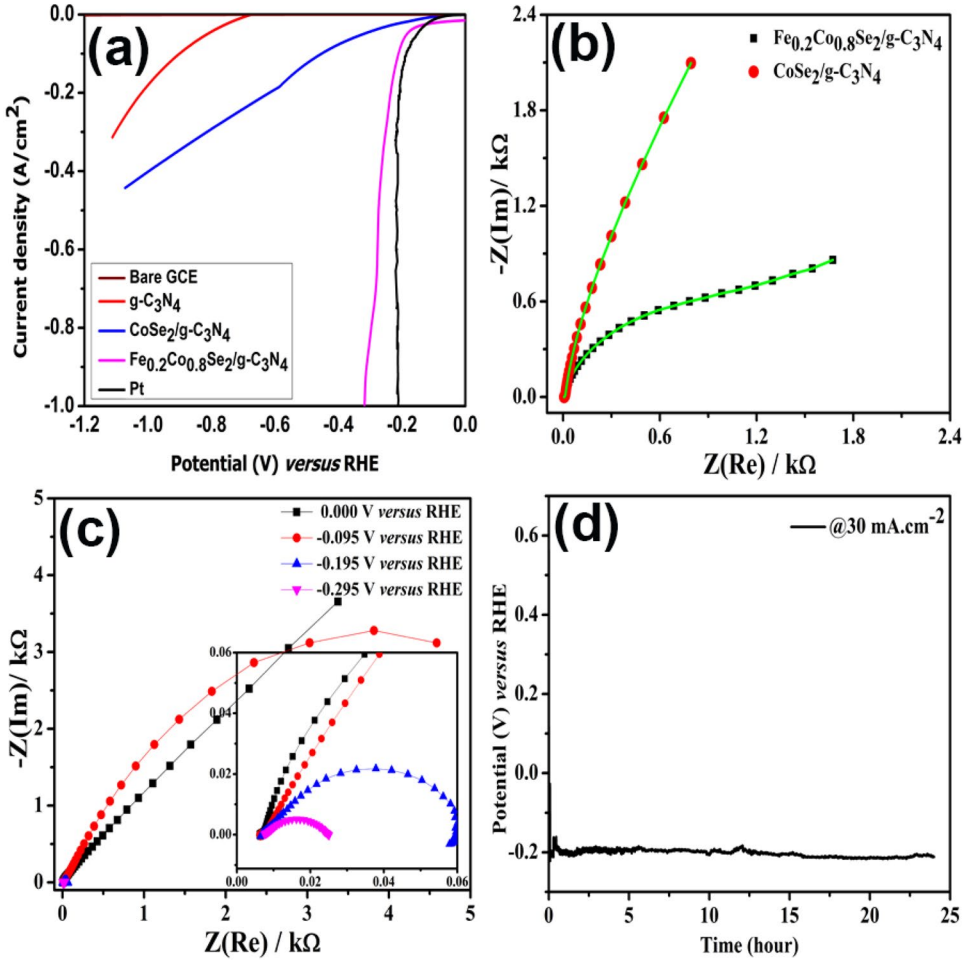

Figure 3. Hydrogen evolution activity of (**a**) bare GCE, g-C_3N_4, $CoSe_2$/g-C_3N_4 and $Fe_xCo_{1-x}Se_2$/g-C_3N_4 and Pt after iR correction in 0.5 M H_2SO_4 (**b**) Nyquist plots for AC impedance measurement of proton conductivity taken under HER working conditions in frequency range of 1000 kHz to 0.1 Hz at 10 mV AC voltage at open-circuit potential (**c**) Nyquist plot of $Fe_{0.2}Co_{0.8}Se_2$/g-C_3N_4 at different biases and (**d**) Stability test of $Fe_{0.2}Co_{0.8}Se_2$/g-C_3N_4 for 24 h in 0.5 M H_2SO_4 (pH 0.3).

H_2 desorption from the electrode surface. The fast desorption soon after production is crucial for industrial applications of electrocatalysts (Supplementary video). However, with further increment of the Fe content after optimal ratio (20 wt%), the HER activity sharply decreased due to its probable changes in electronic configurations. In the same way, the electrocatalytic ability of the $Fe_{0.2}Co_{0.8}Se_2$/g-C_3N_4 was also assessed in DPBS, ASW, 0.1 M H_2SO_4 and 1 M KOH aqueous solutions as shown in Fig. S6b. It is important to note that the relatively high value of -30.12 mA cm^{-2} in 1 M KOH is probably due to a reduction contribution of SeO_3^{2-} species that are generated at the catalyst-electrolyte interface during testing at high pH conditions. The overall performance of $Fe_{0.2}Co_{0.8}Se_2$/g-C_3N_4 is comparable to the benchmark HER electrocatalysts (comparison given in Table S2)[10].

To further investigate the charge transfer behavior at electrode electrolyte interface, the electrochemical impedance spectroscopy (EIS) of $CoSe_2$ and $Fe_{0.2}Co_{0.8}Se_2$ embedded in g-C_3N_4 was performed. It can be seen from the Nyquist plots in Fig. 3b, that $Fe_{0.2}Co_{0.8}Se_2$/g-C_3N_4 had smaller charge transfer resistance (R_{CT}) in comparison with $CoSe_2$/g-C_3N_4, as the arc diameter of $FeCoSe_2$ is smaller than $CoSe_2$ dispersed on substrate. Thus, the EIS of $Fe_{0.2}Co_{0.8}Se_2$/g-C_3N_4 was further performed at different applied potentials. It can be seen from Fig. 3c that the R_{CT} values decrease with increase in applied potential value. Therefore, further increase in applied potential i.e. -0.295 V decreases the R_{CT} and hence enhances the HER activity. Moreover, determining the electrocatalytic active surface area (ECSA) is an important parameter since it shows the intrinsic performance of electrocatalysts. ECSA was calculated by double-layer capacitance (C_{dl}) value (Supplementary note 3) at the electrolyte–electrode interface using cyclic voltammetry (CV given in Fig. S7). As shown in S8, $CoSe_2$ increased the C_{dl} of g-C_3N_4 from 0.20 and 0.52 mF cm^{-2} to 0.85 and 0.56 mF cm^{-2}, respectively at different potential values. After the addition of iron, C_{dl} values rose to 2.73 and 1.20 mF cm^{-2} for $Fe_{0.2}Co_{0.8}Se_2$/g-C_3N_4. These results indicate that the introduction of Fe favorably modulates the ECSAs of $Fe_xCo_{1-x}Se_2$/g-C_3N_4 samples (Table S3).

To assess the stability of $Fe_{0.2}Co_{0.8}Se_2$/g-C_3N_4, chronopotentiometric response was recorded at constant current density of -30 mA cm^{-2} (Fig. 3d). The results show that the composite delivers almost an unchanged

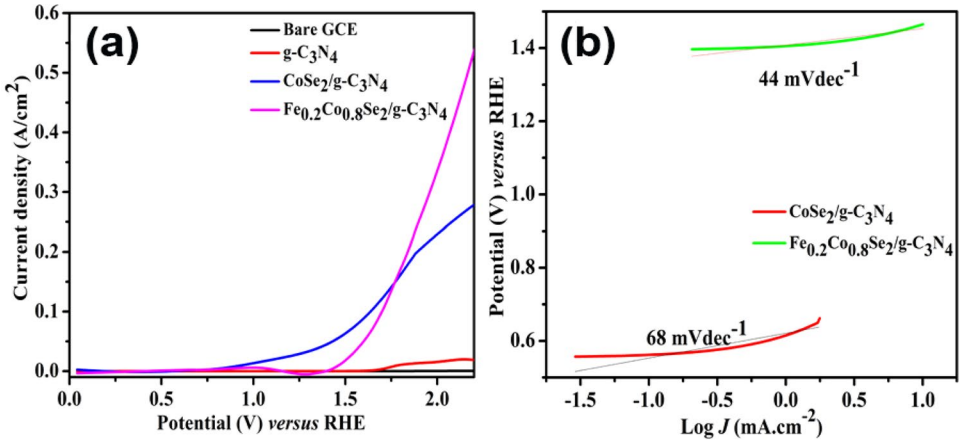

Figure 4. (**a**) OER activity of Bare GCE, g-C_3N_4 and $Fe_xCo_{1-x}Se_2$/g-C_3N_4 in 1 M KOH (**b**) corresponding Tafel slope of $CoSe_2$/g-C_3N_4 and $Fe_{0.2}Co_{0.8}Se_2$/g-C_3N_4 taken at wider potential range in 1 M KOH solution.

potential of −0.2 V at −30 mA cm^{-2} for 24 hours. After long term chronopotentiometric response, the samples were subjected to SEM, EDX and elemental mapping. The analysis (Figs. S9 and 10 and Table S1), confirms that after 24 h of testing the constituent elements in the sample and morphology of the synthesized material remained intact. Further, this elemental analysis of hybrid materials was used to find minimum Turn over frequency (TOF_{min}), (Supplementary note 2) where TOFs of all catalysts reveal that $Fe_{0.2}Co_{0.8}Se_2$/g-C_3N_4 shows highest TOF_{min} (Fig. S6c). All of these results suggest that introduction of iron is of great importance in terms of electrochemical performance as it enhances the charge transfer ability of electrocatalysts and natural hydrogen evolution enzymatic catalysts.

The catalytic activity for oxygen evolution reaction (OER) was investigated in aqueous 1 M KOH solution. $Fe_{0.2}Co_{0.8}Se_2$/g-C_3N_4 showed moderate overpotentials of 230 and 360 mV at 10 and 50 mA cm^{-2}, respectively. The results have been compared with recently reported transition metal chalcogenides based electrocatalysts in Table S4 for OER. Moreover, the synthesized material can deliver high current density of over 500 mA cm^{-2} without any interference from the O_2 bubbles (Fig. 4a). To acquire a direct estimation of intrinsic OER and HER kinetics of electrocatalysts, the Tafel slope was evaluated from the polarization curves. While selecting the region, we avoided very high potentials in order to circumvent oxygen and hydrogen bubble evolution that affects mass transport, and low potentials at which the redox transition for cobalt arises. In each case (i.e., in acidic and alkaline medium), the low Tafel slope of iron incorporated material indicated extremely competitive performance of synthesized material amongst TMDs (Figs. 4b and S11). The Tafel slope values further quantify the enhanced kinetics of charge transfer in the synthesized material.

Conclusions

A low cost and a facile hydrothermal route was adopted for the preparation of $FeCoSe_2$ hybrid uniformly supported on g-C_3N_4 that performed efficiently as a bifunctional electrocatalyst. Introduction of iron was found to be of vital importance as it led to increase in TOF_{min} and electrocatalytic ability of nanohybrid material. Due to optimized Fe incorporation, presence of Se atom and a good conducting substrate, the $Fe_{0.2}Co_{0.8}Se_2$/g-C_3N_4 ensured high ECSAs and enhanced electrocatalytic performance in the context of low overpotential, small Tafel slope, high current density, high proton conductivity, and stability. In addition, the designed catalyst also performed good OER activity with moderate onset potential and high current density values. Due to facile synthesis technique and good electronic properties, g-C_3N_4 can offer a perfect platform for the conversion and modification of catalysts with varied structure and composition. In this work, g-C_3N_4 allowed the catalyst to work in wide pH ranges which is highly desirable for industrial applications. These peculiar qualities imply that $Fe_{0.2}Co_{0.8}Se_2$/g-C_3N_4 hybrid electrocatalyst has the potential to replace benchmark electrocatalysts for clean fuel production in industrial applications.

Received: 24 August 2019; Accepted: 11 March 2020;
Published online: 14 April 2020

References

1. Habas, S. E., Platt, H. A. S., van Hest, M. F. A. M. & Ginley, D. S. Low-cost inorganic solar cells: from ink to printed device. *Chem. Rev.* **110**, 6571–6594 (2010).
2. Steele, B. C. H. & Heinzel, A. Materials for fuel-cell technologies. *Nature* **414**, 345–352 (2001).
3. Wasmus, S. & Küver, A. Methanol oxidation and direct methanol fuel cells: A selective review. *J. Electroanal. Chem.* **461**, 14–31 (1999).
4. Xiao, P., Chen, W. & Wang, X. A review of phosphide-based materials for electrocatalytic hydrogen evolution. *Adv. Energy Mater* **5**, 1500985 (2015).
5. Shi, Y. & Zhang, B. Recent advances in transition metal phosphide nanomaterials: Synthesis and applications in hydrogen evolution reaction. *Chem. Soc. Rev.* **45**, 1529–1541 (2016).
6. Casalongue, H.S., *et al* Direct observation of the oxygenated species during oxygen reduction on a platinum fuel cell cathode. *Nat. Commun.* **4** (2013).

7. Gao, M. R., Xu, Y. F., Jiang, J. & Yu, S. H. Nanostructured metal chalcogenides: Synthesis, modification, and applications in energy conversion and storage devices. *Chem. Soc. Rev.* **42**, 2986–3017 (2013).
8. Lu, F., Zhou, M., Zhou, Y. & Zeng, X. First-row transition metal based catalysts for the oxygen evolution reaction under alkaline conditions: Basic principles and recent advances. *Small* **13**(45), 1701931 (2017).
9. Zeng, Z., Tan, C., Huang, X., Bao, S. & Zhang, H. Growth of noble metal nanoparticles on single-layer TiS_2 and TaS_2 nanosheets for hydrogen evolution reaction. *Energy Environ. Sci.* **7**, 797–803 (2014).
10. Anantharaj, S., Karthik, P. E., Subramanian, B. & Kundu, S. Pt nanoparticle anchored molecular self-assemblies of DNA: An extremely stable and efficient HER electrocatalyst with ultralow Pt content. *ACS Catal* **6**, 4660–4672 (2016).
11. Wang, J. X., Zhang, Y., Capuano, C. B. & Ayers, K. E. Ultralow charge-transfer resistance with ultralow Pt loading for hydrogen evolution and oxidation using Ru@Pt core-shell nanocatalysts. *Sci. Rep* **5**, 12220 (2015).
12. Wang, C., Deķrafft, K. E. & Lin, W. Pt nanoparticles@photoactive metal-organic frameworķs: Efficient hydrogen evolution via synergistic photoexcitation and electron injection. *J. Am. Chem. Soc.* **134**, 7211–7214 (2012).
13. Sun, C. L. *et al*. Ultrafine platinum nanoparticles uniformly dispersed on arrayed CN_x nanotubes with high electrochemical activity. *Chem. Mater.* **17**, 3749–3753 (2005).
14. Song, H. M., Anjum, D. H., Sougrat, R., Hedhili, M. N. & Khashab, N. M. Hollow Au@Pd and Au@Pt core-shell nanoparticles as electrocatalysts for ethanol oxidation reactions. *J. Mater. Chem.* **22**, 25003–25010 (2012).
15. Burķe, M. S., Enman, L. J., Batchellor, A. S., Zou, S. & Boettcher, S. W. Oxygen evolution reaction electrocatalysis on transition metal oxides and (oxy)hydroxides: Activity trends and design principles. *Chem. Mater.* **27**, 7549–7558 (2015).
16. Karan, H. I. *et al*. Catalytic activity of platinum monolayer on iridium and rhenium alloy nanoparticles for the oxygen reduction reaction. *ACS Catal* **2**, 817–824 (2012).
17. Chen, L. Y., Hou, Y., Kang, J. L., Hirata, A. & Chen, M. W. Asymmetric metal oxide pseudocapacitors advanced by three-dimensional nanoporous metal electrodes. *J. Mater. Chem. A* **2**, 8448–8455 (2014).
18. McCrory, C. C. L., Jung, S., Peters, J. C. & Jaramillo, T. F. Benchmarking heterogeneous electrocatalysts for the oxygen evolution reaction. *J. Am. Chem. Soc.* **135**, 16977–16987 (2013).
19. Yingying, G *et al*. Co2P–CoN Double Active Centers Confined in N-Doped Carbon Nanotube: Heterostructural Engineering for Trifunctional Catalysis toward HER, ORR, OER, and Zn–Air Batteries Driven Water Splitting. *Adv. Funct Mater*. **28** (51), 1805641 (1–9) (2018).
20. Groenewolt, M. & Antonietti, M. Synthesis of g-C_3N_4 nanoparticles in mesoporous silica host matrices. *Adv. Mater.* **17**, 1789–1792 (2005).
21. Wang, Y. *et al*. Excellent visible-light photocatalysis of fluorinated polymeric carbon nitride solids. *Chem. Mater.* **22**, 5119–5121 (2010).
22. Logaķis, E. *et al*. Structure-property relationships in isotactic polypropylene/multi-walled carbon nanotubes nanocomposites. *Compos. Sci. Technol* **70**, 328–335 (2010).
23. Benard, D. J. *et al*. Dissociation of cyanogen azide: An alternative route to synthesis of carbon nitride. *J. Phys. Chem. B* **102**, 6010–6019 (2002).
24. Khabashesku, V. N., Zimmerman, J. L. & Margrave, J. L. Powder synthesis and characterization of amorphous carbon nitride. *Chem. Mater.* **12**, 3264–3270 (2000).
25. Bai, X., Cao, C. & Xu, X. Formation and characterization of flower-like carbon nitride by pyrolysis of melamine. *Mater. Sci. Eng. B Solid-State Mater. Adv. Technol* **175**, 95–99 (2010).
26. Xia, X. *et al*. Preparation of magnetic graphitic carbon nitride nanocomposites. *Mater. Lett*. **64**, 2620–2623 (2010).
27. Jiang, G. *et al*. Controllable preparation of graphitic carbon nitride nanosheets via confined interlayer nanospace of layered clays. *Mater. Lett*. **64**, 2718–2721 (2010).
28. Byers, J. C., Tamiasso-Martinhon, P., Deslouis, C., Pailleret, A. & Semenikhin, O. A. Atomic force microscopy studies of carbon nitride (CN_x) films deposited on a conducting polymer substrate. *J. Phys. Chem. C* **114**, 18474–18480 (2010).
29. Xiang, Q., Yu, J. & Jaroniec, M. Preparation and enhanced visible-light photocatalytic H_2- production activity of graphene/C_3N_4 composites. *J. Phys. Chem. C* **115**, 7355–7363 (2011).
30. Cao, S. & Yu, J. g-C_3N_4-based photocatalysts for hydrogen generation. *J. Phys. Chem. Lett.* **5**, 2101–2107 (2014).
31. Ge, L. *et al*. Synthesis and efficient visible light photocatalytic hydrogen evolution of polymeric g-C_3N_4 coupled with CdS quantum dots. *J. Phys. Chem. C* **116**, 13708–13714 (2012).
32. Zhu, T., Chong, M. N. & Chan, E. S. Nanostructured tungsten trioxide thin films synthesized for photoelectrocatalytic water oxidation: A review. *ChemSusChem* **7**, 2974–2997 (2014).
33. Abdullah Khan, M., Teixeira, I. F., Li, M. M. J., Koito, Y. & Tsang, S. C. E. Graphitic carbon nitride catalysed photoacetalization of aldehydes/ketones under ambient conditions. *Chem. Commun.* **52**, 2772–2775 (2016).
34. Anantharaj, S. *et al*. Recent trends and perspectives in electrochemical water splitting with an emphasis on sulfide, selenide, and phosphide catalysts of Fe, Co, and Ni: A review. *ACS Catalysis* **6**, 8069–8097 (2016).
35. Long, A. *et al*. MoS_2 nanosheets grown on nickel chalcogenides: Controllable synthesis and electrocatalytic origins for the hydrogen evolution reaction in alkaline solution. *J. Mater. Chem. A* (2019).
36. Lu, Q. *et al*. Highly porous non-precious bimetallic electrocatalysts for efficient hydrogen evolution. *Nat. Commun.* **6**, 6567 (2015).
37. Tian, J. *et al*. Self-supported NiMo hollow nanorod array: An efficient 3D bifunctional catalytic electrode for overall water splitting. *J. Mater. Chem. A*. **3**(40), 20056–20059 (2015).
38. Xie, J. *et al*. Atomically-thin molybdenum nitride nanosheets with exposed active surface sites for efficient hydrogen evolution. *Chem. Sci* **5**, 4615–4620 (2014).
39. Zhou, M. *et al*. Construction of polarized carbon-nickel catalytic surfaces for potent, durable, and economic hydrogen evolution reactions. *ACS Nano* **12**(5), 4148–4155 (2018).
40. Popczun, E. J. *et al*. Nanostructured nickel phosphide as an electrocatalyst for the hydrogen evolution reaction. *J. Am. Chem. Soc.* **135**, 9267–9270 (2013).
41. Huang, Y. *et al*. Mo_2C nanoparticles dispersed on hierarchical carbon microflowers for efficient electrocatalytic hydrogen evolution. *ACS Nano* **10**, 11337–11343 (2016).
42. Tian, T., Huang, L., Ai, L. & Jiang, J. Surface anion-rich NiS_2 hollow microspheres derived from metal-organic frameworks as a robust electrocatalyst for the hydrogen evolution reaction. *J. Mater. Chem. A* **5**, 20985–20992 (2017).
43. Hu, C. & Dai, L. Multifunctional carbon-based metal-free electrocatalysts for simultaneous oxygen reduction, oxygen evolution, and hydrogen evolution. *Adv. Mater.* **29**, 1604942 (2017).
44. Shi, Y. *et al*. Carbon-nanotube-incorporated graphene scroll-sheet conjoined aerogels for efficient hydrogen evolution reaction. *ACS Sustain. Chem. Eng.* **5**, 6994–7002 (2017).
45. Yu, Y., van Aken, P. A., Maier, J., Zhu, C. & Mu, X. Single-layered ultrasmall nanoplates of MoS_2 embedded in carbon nanofibers with excellent electrochemical performance for lithium and sodium storage. *Angew. Chemie Int. Ed.* **53**, 2152–2156 (2014).
46. Kong, D., Cha, J. J., Wang, H., Lee, H. R. & Cui, Y. First-row transition metal dichalcogenide catalysts for hydrogen evolution reaction. *Energy Environ. Sci.* **6**, 3553–3558 (2013).
47. Kong, D., Wang, H., Lu, Z. & Cui, Y. $CoSe_2$ nanoparticles grown on carbon fiber paper: An efficient and stable electrocatalyst for hydrogen evolution reaction. *J. Am. Chem. Soc.* **136**, 4897–4900 (2014).

48. Liang, H. *et al*. Hydrothermal continuous flow synthesis and exfoliation of NiCo layered double hydroxide nanosheets for enhanced oxygen evolution catalysis. *Nano Lett.* **15**, 1421–1427 (2015).
49. Faber, M. S., Lukowski, M. A., Ding, Q., Kaiser, N. S. & Jin, S. Earth-abundant metal pyrites (FeS_2, CoS_2, NiS_2, and their alloys) for highly efficient hydrogen evolution and polysulfide reduction electrocatalysis. *J. Phys. Chem. C* **118**, 21347–21356 (2014).
50. Faber, M. S. *et al*. High-performance electrocatalysis using metallic cobalt pyrite (CoS_2) micro- and nanostructures. *J. Am. Chem. Soc.* **136**, 10053–10061 (2014).
51. Zhou, M. *et al*. *In situ* electrochemical formation of core-shell nickel-iron disulfide and oxyhydroxide heterostructured catalysts for a stable oxygen evolution reaction and the associated mechanisms. *J. Mater. Chem. A* **5**, 4335–4342 (2017).
52. Akhtar, M., Malik, M. A., Raftery, J. & O'Brien, P. Synthesis of iron selenide nanocrystals and thin films from bis(tetraisopropyldiselenoimidodiphosphinato)iron(II) and bis(tetraphenyldiselenoimidodiphosphinato)iron(II) complexes. *J. Mater. Chem. A* **2**, 20612–20620 (2014).
53. Cook, P., Kim, Y. J., Yuan, K., Marcano, M. C. & Becker, U. Electrochemical, spectroscopic, and computational investigations on redox reactions of selenium species on galena surfaces. *Minerals* **9**, 437 (2019).
54. Basu, M. *et al*. $CoSe_2$ embedded in C_3N_4: An efficient photocathode for photoelectrochemical water splitting. *ACS Appl. Mater. Interfaces* **8**, 26690–26696 (2016).

Acknowledgements

Aamir Hassan Shah from CAS Laboratory of Nanosystem and Hierarchical Fabrication, CAS Center for Excellence in Nanoscience, National Center for Nanoscience and Technology, China is acknowledged for his valuable suggestions to improve the manuscript.

Author contributions

Muhammad Zulqarnain, Afzal Shah and Faiza Jan Iftikhar designed and performed electrode modification experiments, electrochemical study for its catalytic role and characterization of the synthesized catalyst such as FTIR and DSC/TGA. Muhammad Zulqarnain, Muhammad Abdullah Khan and Afzal Shah contributed in writing the manuscript. Afzal Shah and Muhammad Abdullah Khan characterized the modified electrode by XRD, EDX and SEM along with contribution in analysis of results. Jan Nisar was involved in characterization of TEM and revision of the manuscript. All authors reviewed the manuscript.

Competing interests

The authors declare no competing interests.

Additional information

Supplementary information is available for this paper at https://doi.org/10.1038/s41598-020-63319-7.

Correspondence and requests for materials should be addressed to A.S.

Reprints and permissions information is available at www.nature.com/reprints.

Publisher's note Springer Nature remains neutral with regard to jurisdictional claims in published maps and institutional affiliations.

Open Access This article is licensed under a Creative Commons Attribution 4.0 International License, which permits use, sharing, adaptation, distribution and reproduction in any medium or format, as long as you give appropriate credit to the original author(s) and the source, provide a link to the Creative Commons license, and indicate if changes were made. The images or other third party material in this article are included in the article's Creative Commons license, unless indicated otherwise in a credit line to the material. If material is not included in the article's Creative Commons license and your intended use is not permitted by statutory regulation or exceeds the permitted use, you will need to obtain permission directly from the copyright holder. To view a copy of this license, visit http://creativecommons.org/licenses/by/4.0/.

© The Author(s) 2020